# TOMOGRAPHIC RECONSTRUCTIONS OF PHOTOELECTRON DISTRIBUTIONS FROM STRONG-FIELD IONIZATION IN TWO-COLOR CIRCULARLY POLARIZED LIGHT FIELDS

Maithreyi Gopalakrishnan
Kapteyn-Murnane Group
JILA Physics, University of Colorado-Boulder
Thesis Defense Date: March 16th, 2015
Advisers: Dr. Henry Kapteyn and Dr. Margaret Murnane
Adviser Department: Physics/Engineering Physics
Honors Council Representative: Dr. Jun Ye
Honors Council Representative Department: Physics
External Committee Member: Dr. Angela Thieman-Dino
External Committee Member Department: Leadership

# Abstract

In this experiment, we propagate superposed 800 nm and 400 nm circularly polarized driving laser fields and interact the combined field with argon gas—in doing so, we demonstrate strong field ionization from this interaction. We then use velocity map imaging and tomographic reconstruction techniques to look at the resulting photoelectron angular distributions. From this, we discover that if the driving fields are counter-rotating, we see low energy structures which indicate rescattering of electrons off of their parent atoms. The presence of these low energy structures offers the first experimental verification of the theoretical model describing how circularly polarized high harmonics are generated. I discuss in this thesis: the concepts of high harmonic generation and strong field ionization, the interest in circularly polarized driving laser fields for producing circularly polarized high harmonics, applications of circular x-ray light, a detailed explanation of our experiment, the specific role that I played, our results, and current projects and extensions to this experiment that I am working on presently.

# Contents

# I. Objective

In this research, we utilize a two-color circularly polarized driving laser field interacting with a gas to observe the process of strong field ionization (SFI). A tomographic reconstruction of the data collected from this process allows us to develop three-dimensional photoelectron momentum distributions, from which we can physically see final drift momenta of ionized electrons weighted by the driving electric field. The two colors in the driving field can either be set to rotate in the same direction (co-rotating) or in opposite directions (counter-rotating). In the latter case, we note the presence of low energy structures in the three-dimensional distributions, which indicates that re-scattering of electrons off of the parent atoms from which they were ionized occurs. This suggests that high harmonic generation (HHG), the sister process of SFI, can take place, and experimentally verifies why circular harmonics in the counter-rotating case can be produced. Our research and findings pave the way for new studies of atomic and molecular dynamics that could not have been performed with linear EUV light.

# II. Motivation

## A. Imaging on Short Time Scales

For what purpose do we choose to use femotosecond lasers for our experiment? They are tools for studying dynamics that we seek to learn more about. Different processes and phenomena occur on different time scales. For example, the chain reaction of a nuclear explosion is on the order of nanoseconds ($10^{-9}$ seconds) [1], the switching time for the fastest transistor in the world is a few picoseconds ($10^{-12}$ seconds) [2], and electron dynamics typically happen on a femtosecond ($10^{-15}$ seconds) to attosecond ($10^{-18}$ seconds) time scale [3]. To be able to image processes on these shorter time scales, it is necessary to have exposure times close to the time scales on which the processes occur. Additionally, for our experiment specifically, we need high peak pulse powers to cause SFI, and because peak power is inversely proportional to pulse duration, shorter pulse durations will allow us to achieve the peak powers that we require. For these reasons, we use pulsed lasers with pulse durations of tens of femtoseconds. With these lasers, we can image electron dynamics and reach the peak pulse powers needed to instigate SFI.

## B. What Can Be Studied With Two-Color Circularly Polarized Fields?

Further along in my thesis, I will go into details as to why we must use two-color circularly polarized driving laser fields. For now, it is enough to know that circular driving laser fields have the distinct advantage that in SFI, they clearly separate electrons that are rescattered from electrons that are ionized but do not rescatter. Another reason to use circular driving fields is that driving fields of this nature, under certain circumstances, can efficiently produce circularly polarized EUV or x-ray light, which is a very powerful tool that can be utilized for several applications. The two that I will discuss are X-Ray Magnetic Circular Dichroism and studying chirality in molecules. I will briefly summarize these applications below, and delve into further detail about each application in the following section of my thesis.

### 1. X-Ray Magnetic Circular Dichroism

X-Ray Magnetic Circular Dichroism (XMCD) is a technique utilized to better understand the magnetic properties of a material. This technique requires the use of circularly polarized x-ray

light, as it takes a difference between two absorption spectra. If the light is circularly polarized in one direction, then all of the spins in the material will align to be up, or down, depending on the direction that the light is circularly polarized. Using XMCD, one can gain more knowledge regarding properties of a magnetic material, such as its spin and its magnetic moment [4].

### 2. Chirality in Molecules

Using a similar technique in measuring absorption as is done in XMCD, circular EUV or x-ray light can also be utilized to determine whether a molecule is chiral. If the difference in absorption between left and right circularly polarized light is nonzero, it can be concluded that the molecule absorbing the light is chiral. This technique can be employed to study the structures of these molecules and their movement, as well [5].

## III. Background

### A. High Harmonic Generation and Strong Field Ionization

In our lab, we generate x-ray light using high harmonic generation (HHG). This is a nonlinear process that essentially multiplies the frequency of a driving laser field to achieve higher frequency coherent light sources. The simplest case of this is second harmonic generation (SHG), where the outgoing light has double the frequency of the incoming light. However, HHG can reach much higher frequencies than simply twice the driving field frequency, which is what allows us to use it to create x-ray light [6]. HHG is a specific case of strong field ionization (SFI), where a strong field interaction with an atom tunnel-ionizes an electron. SFI is most effectively summarized by a three-step model of ionization, acceleration, and not returning/rescattering/recombining. This model, including the three possibilities of what can happen to the electron after recombination, is shown in Figure 1.

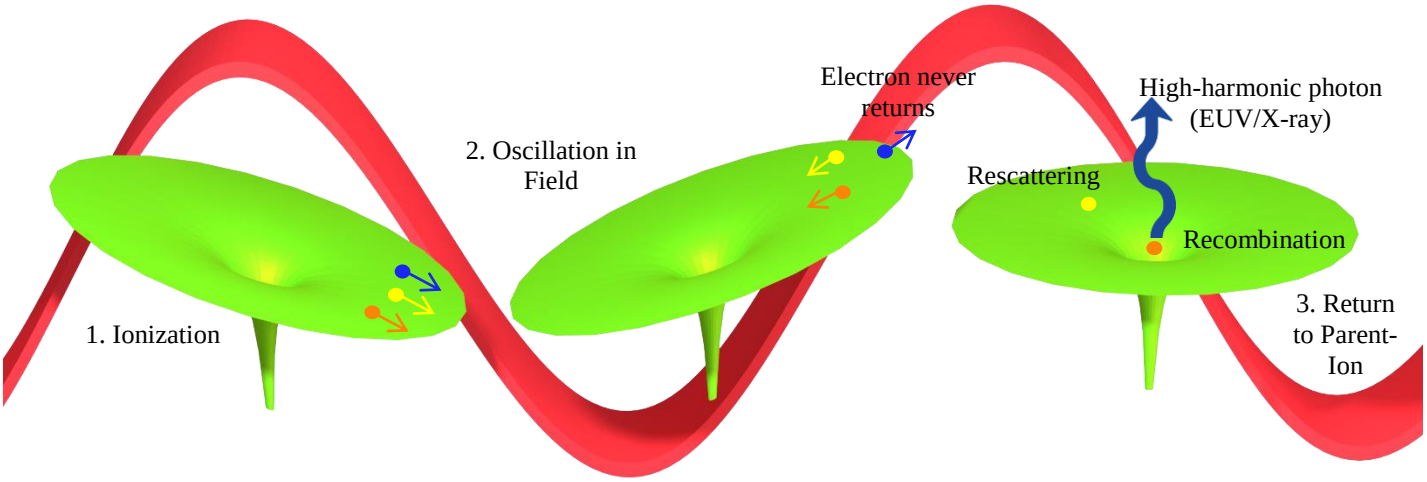


Figure 1
(Hickstein, 2015)
The three step model of strong field ionization, where the ionized electron either misses the parent atom completely, rescatters off the parent atom, or recombines with the parent atom and emits a high energy photon.

In the three-step model, an electron that sits in the Coulomb potential of its parent atom is ionized by an incoming driving laser field. Ionization can occur because the potential of the driving field superposed with that of the parent atom results in an asymmetric potential. This allows the electron to tunnel out of the potential well it sat in, and to travel in the driving laser field. In the field, the electron accelerates, and therefore gains energy. After this step, the electron can do one of three things. It can: travel away and not return to the parent atom, rescatter off of the parent atom, or recombine with the parent atom. In the latter two scenarios, the electron travels back toward its parent atom on every half cycle of the driving laser field when the field changes directions. Recombination can only occur if particular conditions are met, and the probability that the electron will recombine is $10^{-6}$. If recombination does occur, the electron's energy gets transferred to a photon of light at a higher energy than the photons of the driving laser field, since the ionized electron acquires energy in the acceleration phase of HHG [7].

The conditions allowing for recombination in the linear case can be derived from the equation for the simple case of the electric field of an incoming linearly polarized beam. We will define this field as:

$$E(t) = E_o \cos(\omega_o t)$$

We will rename the $\omega_o t$ as a phase term $\theta$ and introduce an initial condition $\theta_i = \omega_o t_i$, where $t_i$ is the time at which the electron is ionized from the parent atom. These phase terms will be substituted into our trajectory equation once it has been derived. Additionally, we will introduce the term $t'$ as a dummy variable when integrating for the electron motion. This motion can be found with the following sequence of steps, with all non-standard quantities (i.e. electron mass and charge) having already been defined.

$$F = ma = -eE \qquad\qquad a = \frac{dv}{dt} = -\frac{eE}{m_e}$$

$$v(t) = -\int_{t_i}^{t} \frac{e\,E(t)}{m_e} dt = -\int_{t_i}^{t} \frac{e\,E_o}{m_e} \cos(\omega_o t') dt = -\frac{e\,E_o}{m_e\,\omega_o} (\sin(\omega_o t) - \sin(\omega_o t_i))$$

$$z(t) = \int_{t_i}^{t} -\frac{e\,E_o}{m_e\,\omega_o} (\sin(\omega_o t') + \sin(\omega_o t_i)) dt$$

$$= \frac{e\,E_o}{m_e\,{\omega_o}^2} (\cos(\omega_o t) - \cos(\omega_o t_i)) + (t - t_i) \frac{E_o}{\omega_o} (\sin(\omega_o t_i))$$

$$z(\theta) = \frac{e\,E_o}{m_e\,{\omega_o}^2} [\cos(\theta) - \cos(\theta_i) + (\theta - \theta_i)(\sin(\theta_i))]$$

The kinetic energy of the electron is given by the equation:

$$E_{kin}(\theta) = \frac{1}{2} m_e v^2 = \frac{1}{2} m_e \left( -\frac{e\,E_o}{m_e\,\omega_o} (\sin(\theta) - \sin(\theta_i)) \right)^2 = \frac{1}{2} \frac{e^2 {E_o}^2}{{m_e}^2\,{\omega_o}^2} (\sin(\theta) - \sin(\theta_i))^2$$

$$= 2\,\mathcal{U}_p (\sin\theta - \sin\theta_i)^2$$

In the above equation, $\mathcal{U}_p = \frac{e^2 {E_o}^2}{4\, m^2\, {\omega_o}^2}$ is defined as the ponderomotive energy of the electron. After substituting the recombination phase $\theta_r$ for the phase $\theta$, numerical methods can be employed to determine that the initial phase must be within the limits of $0 < \theta_i < \frac{\pi}{2}$. If the initial phase is instead in the range of $\frac{\pi}{2} < \theta_i < \pi$, the electron cannot recombine with its parent atom, preventing HHG from taking place. This condition is shown graphically in Figure 2.

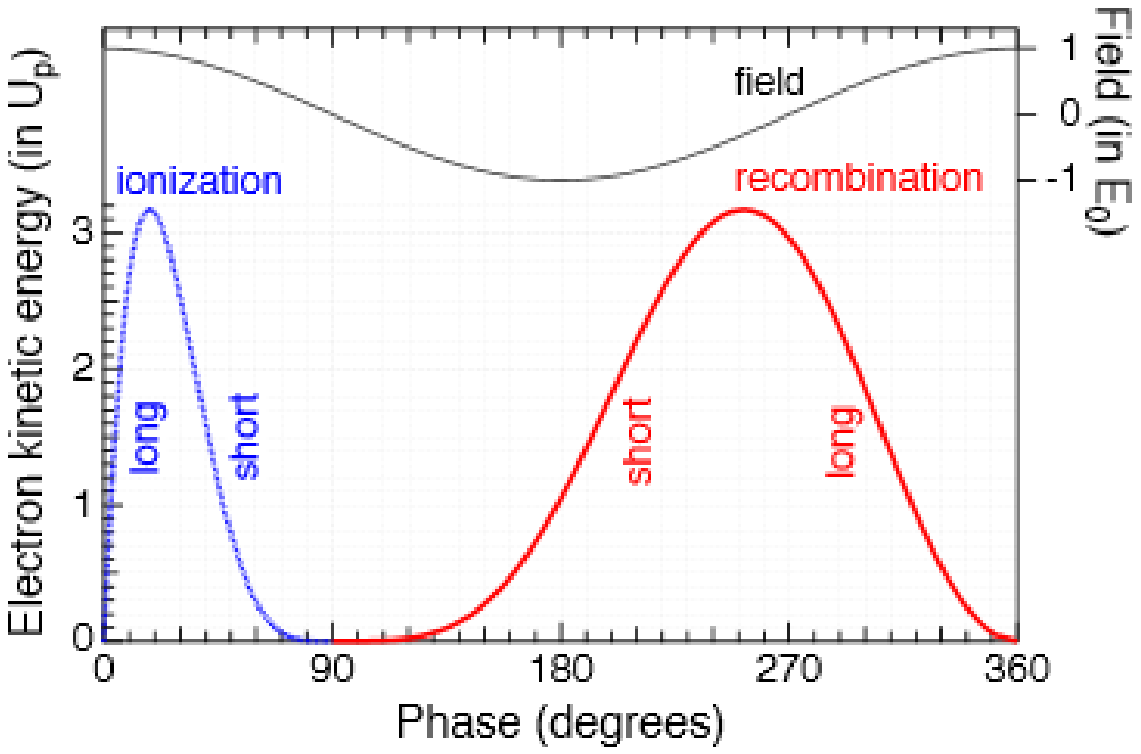


Figure 2
(Ishikawa, 2010)

Electron kinetic energy as a function of phase angle. In the short trajectory of the ionized electron, recombination can occur if the initial phase angle is between 0 and 90 degrees, and the electron kinetic energy is at or below $3.17U_p$.

This graph, in addition to demonstrating the aforementioned condition of initial phase angle, also shows the condition for the maximum kinetic energy of the recombining electron. That maximum energy is $3.17\mathcal{U}_p$, and can be derived from the initial phase angle condition using numerical methods in MATLAB. Therefore, the total cutoff energy for the recombining electron is $3.17\mathcal{U}_p + I_p$, $I_p$ here being the ionization potential of the parent atom—in other words, if the total energy of the ionized electron is higher than this cutoff value, the electron cannot recombine with its parent atom [8]. The final condition I will discuss is that the electron can only recombine on every half cycle of the driving laser pulse. This can be attributed to the fact that the driving field must flip in order for the electron to turn around with the field and recombine. Figure 3 below illustrates this condition, showing harmonics that occur at the peaks and troughs of the fundamental field, the points at which this field changes directions.

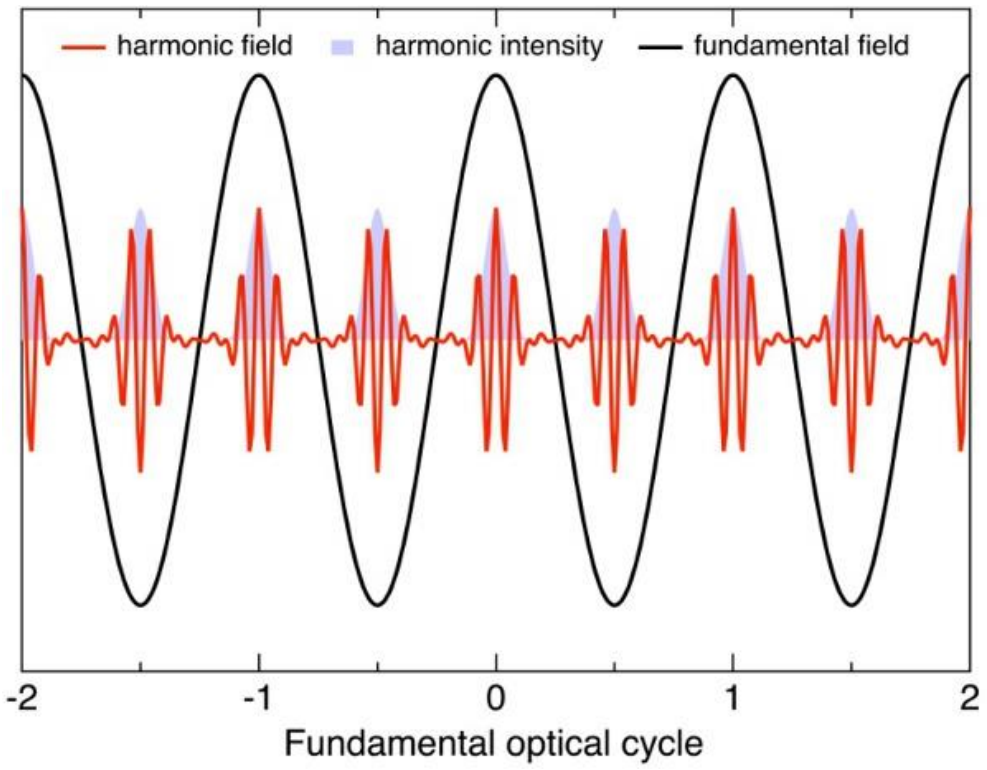


Figure 3
(Ishikawa, 2010)
Electric field of driving laser (fundamental field) and electric field of high harmonics (harmonic field). The peaks of the harmonic field occur at the points when the driving laser field flips direction, indicating that this field-flipping is a condition for bright high harmonics to be produced.

## B. Theory of two-color circularly polarized driving laser fields

All of the conditions for electron recombination that were specified in the previous section are detailed for the case in which the driving laser field is linearly polarized. In this case, the velocity components of the ionized electron are:

$$v_x = v_o \sin(\omega t) \qquad v_y = 0$$

Here, $v_{o_x}$ and $v_{o_y}$ are the electron's initial x and y velocities, respectively. We can integrate the above equations, to obtain the x and y components of the electron trajectory, as shown below:

$$z_x(t) = \int v_o \sin(\omega t)\, dt = \frac{-v_o}{\omega}\cos(\omega t) + z_{x_i}$$

$$z_y(t) = \int 0 dt = z_{y_i}$$

From these trajectory equations, we can see that in the linear case, only one component of the trajectory has sinusoidal elements. This implies that the electron will oscillate in the driving laser field, but will return toward the parent atom in a linear trajectory so can recombine.

If, however, the electron is traveling in an elliptical or circular trajectory, the velocity components of the ionized electron are instead given by:

$$v_x = v_o \sin(\omega t) \qquad v_y = \pm\alpha\, v_o \cos(\omega t)$$

In the above y component of the velocity, $\alpha$ represents the ellipticity of the driving laser field, with $\alpha = 0$ being the linearly polarized case and $\alpha = 1$ being the circularly polarized case. These equations can be integrated to obtain the trajectory equations as follows:

$$z_x(t) = \int v_o \sin(\omega t)\, dt = \frac{-v_o}{\omega}\cos(\omega t) + z_{x_i}$$

$$z_y(t) = \int \pm\alpha\, v_o \cos(\omega t)\ dt = \pm\alpha \frac{v_o}{\omega}\sin(\omega t) + z_{x_i}$$

Both the x and the y components of the electron trajectory in this case contain sinusoidal components, so the rate of recombination is dependent on the ellipticity of the driving laser field. In the circular case where $\alpha = 1$, there is no chance that recombination will occur, since the coefficients in front of the cosine and sine components are equal [10]. This functional dependence of harmonic yield (correlated to recombination rate) on ellipticity is demonstrated in Figure 4 [11].

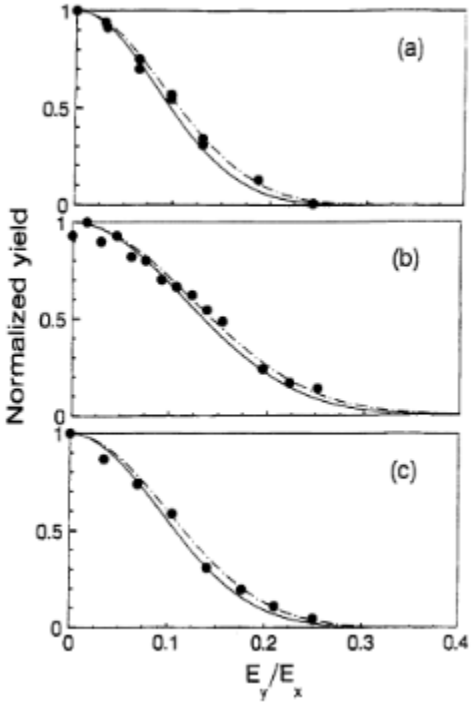


Figure 4
(Dietrich *et al*, 1994)
Theory versus experiment plots of normalized photon yield with respect to ellipticity of driving laser field. The plots shown are of harmonics of (a) Neon, (b) Argon, and (c) correlated ionization yield.

This suppression of harmonics for larger ellipticities of the driving laser field would seemingly limit the possibility of generating circularly polarized EUV light, which is desirable to generate for important applications. However, if we consider utilizing more than one wavelength of light in the driving laser field, we find that it is indeed possible to produce circularly polarized high harmonics. We can combine two driving fields at different frequencies, and are polarized in either the same direction (co-rotating) or in opposite directions (counter-rotating). In our experiment, we use two fields with frequencies $\omega_1$ and $\omega_2$, where $\omega_2 = 2\omega_1$, but the two light fields can have any frequency. For the fields where $\omega_2 = 2\omega_1$, the velocity components of the ionized electron, assuming no initial velocity, are, for the counter-rotating case:

$$v_x = v_o \sin(\omega t) + v_o \sin(-2\omega t) \qquad v_y = v_o \cos(\omega t) + v_o \cos(-2\omega t)$$

And for the co-rotating case:

$$v_x = v_o \sin(\omega t) + v_o \sin(2\omega t) \qquad v_y = v_o \cos(\omega t) + v_o \cos(2\omega t)$$

The resultant electric field for the counter-rotating case is a trefoil, and the field for the co-rotating case is a cardioid. These fields will be shown later in the experimental setup section of this paper. Figure 5 shows a theoretical prediction of harmonic intensity as a function of harmonic order [12].

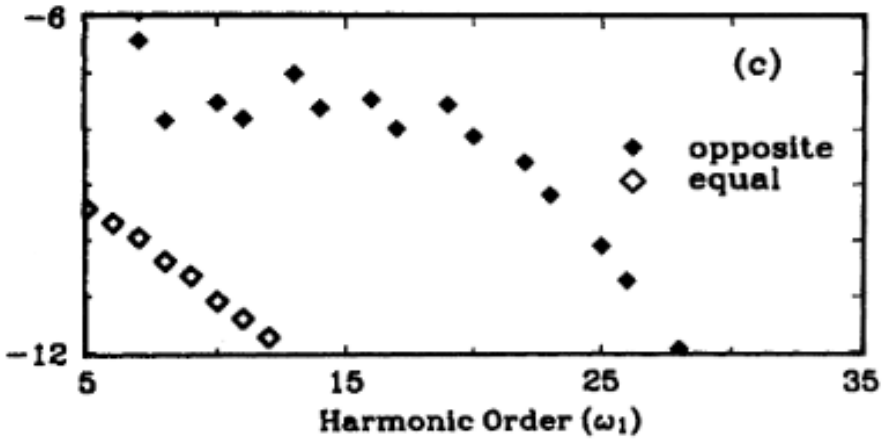


Figure 5
(Long *et al*, 1995)
This is a plot of $\log_{10}(|L(\Omega)^2)$ versus harmonic order for $\omega_2=2\omega_1$, for a two-color circularly polarized driving laser field. They y axis is a representation of intensity of the harmonic field. The solid diamonds labeled "opposite" are for the counter-rotating case, and the open diamonds labeled "equal" are for the co-rotating case.

As can be extrapolated from this figure, harmonics are further suppressed in the co-rotating case than in the counter-rotating case. This is a product of conservation of energy and spin of circularly polarized light. The former condition dictates that for a certain number of photons that are absorbed by an electron ionized in HHG, the high-photon released in the process must contain the same energy as the collective photons that initially ionized the electron contained. The latter condition says that each photon of circularly polarized light must be either a spin +1 photon or a spin -1 photon. So, the x-ray photons emitted in HHG must have spin +1 or -1. The spin of the high harmonic photon is the sum of the spins of the photons that ionized an electron in the first place. In the counter-rotating case, the driving field has some photons with spin +1 and some photons

with spin -1. Therefore, it is possible for the sum of the spins of the driving photons to be +1 or -1, allowing the spin of the x-ray photon to be +1 or -1. In the co-rotating case, however, all of the photons in the driving field will have either spin +1 or spin -1, so it is not possible to sum these spins together to obtain a +1 or -1 total spin, and thus not possible for circularly polarized harmonics to be generated [12]. This is the theory behind why two-color counter-rotating circularly polarized driving laser fields have the potential to generate bright circularly polarized high harmonics. Experimental proof of why this is possible will be shown through the data from our lab that I will present in the "Results" section of this paper.

### C. Experimental circularly polarized high harmonics

The most straightforward experimental method shown to generate circular high harmonics was to make linearly polarized harmonics from a linearly polarized driving field, then circularly polarize the harmonics with a four-reflector phase-shifter. For the experiment that made circular harmonics in this way, the driving laser was a Ti:Sapphire, with an 815 nm wavelength, 1 kHz repetition rate, and 40 femtosecond pulse duration. Though this experiment did produce circularly polarized EUV light, the four-reflector phase shifter was only designed for a single wavelength of light, so this would need to be replaced with a different phase shifter for any other desired harmonic frequencies. Additionally, the method was rather lossy, with only a 2.6-4.4% conversion efficiency [13]. This was because optics designed to work at these higher frequencies are more absorptive, so there are more losses from these optics.

An alternate setup for producing circularly polarized high harmonics, employing the concept of two-color circularly polarized driving laser fields discussed in the previous section of this paper, is shown in Figure 6.

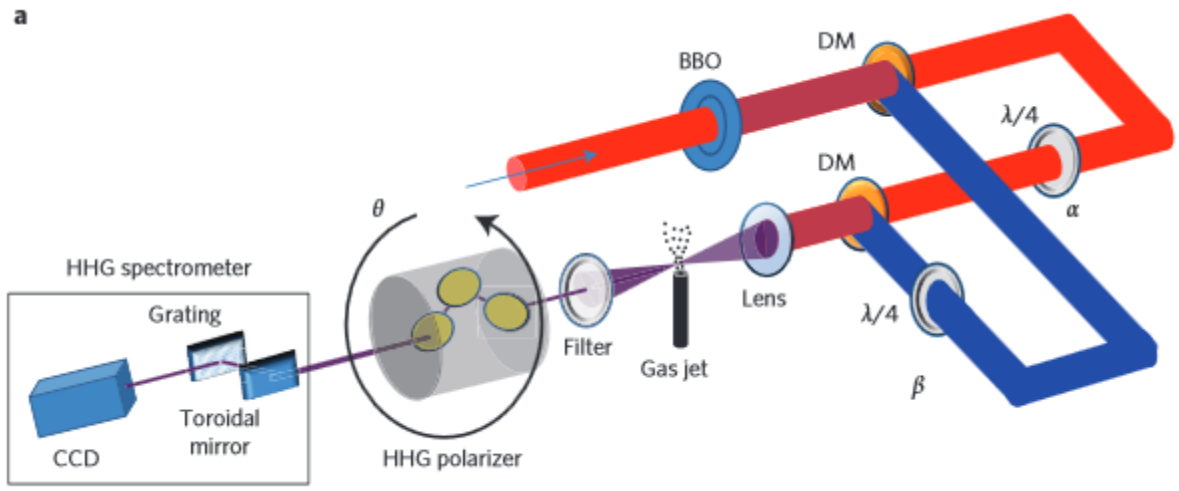


Figure 6
(Fleischer *et al*, 2014)
A setup for generating circularly polarized high harmonics with a two-color circularly polarized driving field.

In this experiment, a Ti:Sapphire laser with a 1 kHz repetition rate, 40 femtosecond pulse duration, and 2 mJ pulse energy was utilized. The driving field is a combination of an 800 nm light (shown

in red) and a 410 nm light (shown in blue), the 410 nm light being produced by a BBO doubling crystal. Both beams are focused to an intensity of approximately $2 \times 10^{14}\ {}^{W}/_{cm^2}$. The setup in Figure 7 successfully produces circularly polarized EUV light when the two driving fields are counter-rotating, without compromising efficiency as was the case for the aforementioned experiment where linear harmonics were circularly polarized. One element needed to make this experiment work is phase-matching. Only if the driving field is phase matched with the harmonic field will the harmonics be as bright as can be obtained [14]. A significant advantage of the setup in Figure 7 is that the polarization of the harmonics generated is entirely dependent on the polarization of the driving laser field. This implies that if elliptical (but not perfectly circular) harmonics are desired, a simple turn of the $\lambda/4$ waveplates in the setup will change the ellipticity of the EUV light produced. Circular harmonics produced in this way can be utilized for a number of applications, including studies in magnetics and molecular structures. This setup is very similar to the setup that we use to produce SFI from a two-color circularly polarized driving laser field. The only difference is that we observe the electrons that were ionized from their parent atoms but did not recombine, while this experiment observes the intensities of the high harmonics produced.

### D. Applications of circular HHG

Two of the most studied areas where circular EUV or soft x-ray light is an essential tool are chirality in molecules and magnetic material properties. Studying both areas requires the technique of circular dichroism, and the fact that we can now produce circular harmonics using a tabletop source allows for these experiments to be conducted in a smaller-scale laboratory rather than at a large user facility.

The two-color circular setup shown in Figure 7 was used to measure x-ray magnetic circular dichroism (XMCD) of a cobalt film. XMCD is a technique that measures the absorption spectrum of a material when the EUV light hitting it is circularly polarized in one direction versus in the other direction. A difference spectrum between the two measured spectra is created and analyzed to better understand particular properties of a magnetic material like cobalt. Examples of such properties measured in this experiment include the harmonic spectrum transmitted through cobalt and its dependence on the magnetization of cobalt, the XMCD asymmetry (or difference spectrum between the intensities of harmonics when the cobalt's magnetization is up versus down), and absorption edges of different materials. X-ray light is required for this application in order to achieve the photon energies needed to probe the absorption edges of the materials being studied. For example, the absorption edge for iron and cobalt is around 45 eV, so the high harmonic photons directed at samples of these materials must have comparable energies [4]. A graph of the absorption spectra and asymmetry are shown in Figure 7.

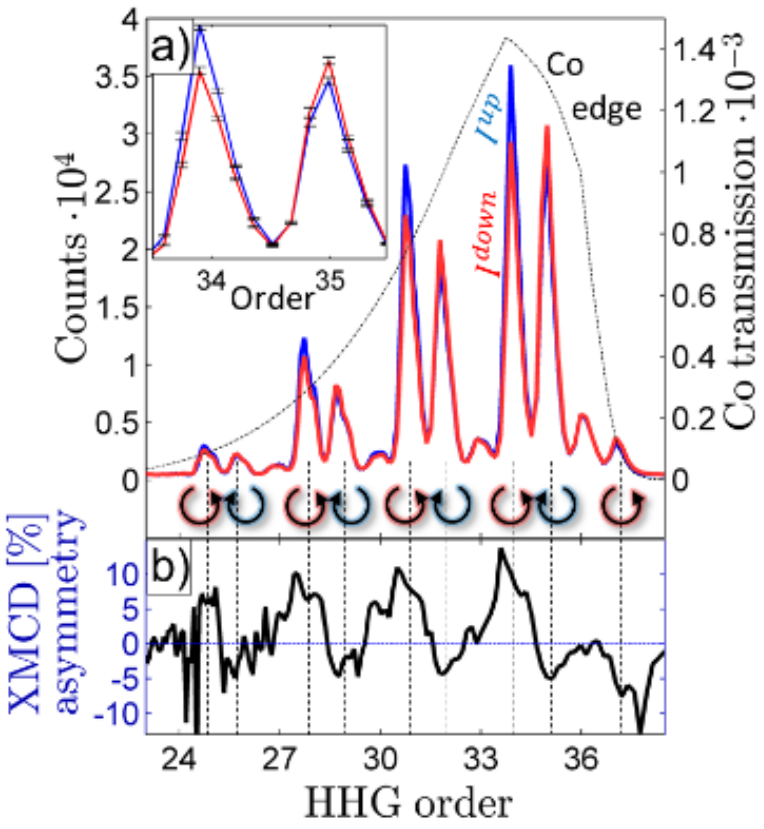


Figure 7
(Kfir *et al*, 2014)

(a) Absorption spectrum of cobalt when the harmonic beam is right circularly polarized versus left circularly polarized, with the red and blue arrows indicating the direction of polarization of the harmonics created. (b) Asymmetry of cobalt as a function of harmonic order, which is the difference spectrum between the two spectra shown in figure 8a.

Chirality in molecules is another topic that circular dichroism can be utilized for. The fundamental equation for circular dichroism (which is also applicable to the XMCD case) is:

$$\Delta A(\lambda) = A(\lambda)_{LCPL} - A(\lambda)_{RCPL}$$

In this equation, $A$ is the absorption of the EUV light by the material, molecule, etc. LCPL and RCPL stand for left circularly polarized light and right circularly polarized light, respectively, and $\lambda$ is the wavelength of EUV light. If a molecule is chiral, then $\Delta A(\lambda) \neq 0$, while if the molecule is not chiral, $\Delta A(\lambda) = 0$. This occurs because chiral molecules are characterized by circular birefringence, where a solution of a chiral molecule becomes a medium through which left circularly polarized light and right circularly polarized light propagate at different speeds [5]. Identifying whether a molecule is chiral can be done even with circularly polarized light in the visible wavelength range, but circularly polarized x-ray light allows us to see electronic transitions in chiral molecules.

In addition to magnetic material properties and molecule chirality, circularly polarized EUV light can be employed to study quantum phases in particular types of insulators, as well as molecular decay [4].

# IV. Experiment

## A. Setup

The setup for this experiment is shown in Figure 8 below [15].

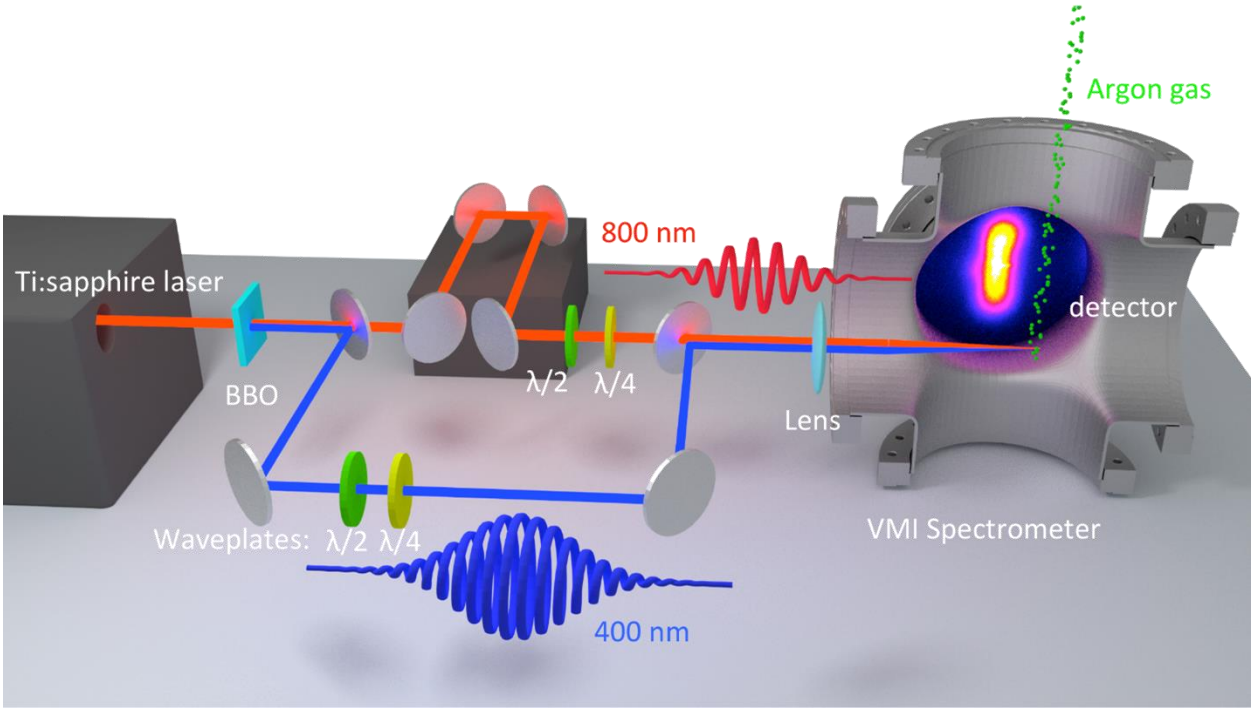


Figure 8
(Mancuso & Hickstein, 2014)
Our experimental setup for producing strong field ionization from combined 800 nm and 400 nm circularly polarized driving laser fields.

We start with a pulse from an 800 nm (for our setup, 790 nm), 45 fs Ti:Sapphire laser, shown as the red beam in the figure. This light is sent through a beta barium borate (BBO) crystal to upconvert part of the 800 nm beam to 400 nm (395 nm in our setup). Both the 800 nm beam and the 400 nm beam have intensities of 5 x $10^{13}$ W/cm$^2$. A dichroic mirror splits the 800 nm beam and 400 nm beam into two separate arms, after which λ/4 and λ/2 waveplates are put in each beam line to circularly polarize the beams. Part of the 800 nm arm is also put on a translation stage, which I will explain in further detail in the following part of this section. A second dichroic mirror recombines the two beams, the two dichroic mirrors creating a Mach-Zehnder interferometer. As discussed in an above section of this paper, the superposition of the two circularly polarized fields results in either a trefoil or a cardioid field. The combined field is then focused into the velocity map imaging (VMI) spectrometer chamber with a lens, and interacts with argon from a gas jet at

its focus point [16]. This is when strong field ionization occurs, and the ionized electrons are redirected toward a detector (I will explain how this redirection takes place in the following part of this section). It will be important to note that the bottom part of the chamber is in vacuum on the order of $10^{-7}$ torr.

### 1. The role of phase delay

The combined driving electric field and corresponding potentials in the counter-rotating and co-rotating cases are shown in Figure 9. Note that both fields have the same intensity.

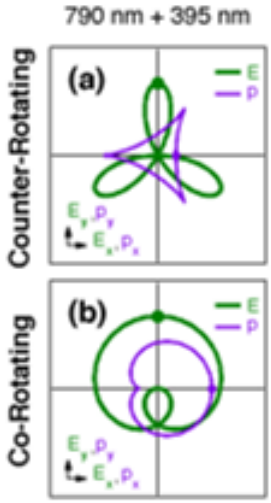


Figure 9
(Mancuso *et al*, 2015)
Combined electric field (E) and final momentum (p) of 790 nm and 395 nm circularly polarized driving laser fields in (a) counter-rotating and (b) co-rotating case. The three maxima in E correspond to minima in p in (a), while the single maximum in E correspond to a maximum in p in (b).

The trefoil pattern in the counter-rotating case and cardioid pattern in the co-rotating case are seen in this figure. However, if we turn the trefoil or cardioid to be in and out of the page rather than facing us, we would see what the detector sees—a profile view with greater intensity at some points than at others. This is because the trefoil or cardioid propagates through the VMI perpendicular to the detector. Thus, we cannot directly image the patterns of electrons ionized from their fields. Instead, we use a process called tomographic reconstruction, which correlates an image on the detector to a phase angle and performs a three-dimensional reconstruction of the full "object"—here, the electrons being ionized from by the driving laser—being imaged. If the 800 nm and 400 nm beams maintain the same relative phase throughout the data-taking process, the detector will see the same two-dimensional profile view of the trefoil or cardioid repeatedly. However, if we incrementally change the relative phase between the two beams, then the trefoil or cardioid will rotate, allowing the detector to capture a different two-dimensional profile of the ionized electrons at each different delay between the 800 nm and 400 nm beams. Since we will have a different image at each phase delay, our tomographic reconstruction of the photoelectron distribution will work in reconstructing the three-lobed or single-lobed structures. In our setup, we

induce this varying phase delay by using the translation stage shown in Figure 9 to change the phase of the 800 nm beam relative to that of the 400 nm beam.

## B. My role

I worked on several parts of this experimental setup, particularly on the VMI side. With the help of lab mates, I built up and tested the VMI spectrometer chamber, which allowed imaging of SFI to take place. Additionally, I set up the optics to steer the two circularly polarized beams, overlapped, through a lens and into the chamber. To acquire and store data, I also modified a program in LabView that controlled the camera and translation stage that we used.

### 1. Velocity map imager

In this experiment, we use an Eppink-Parker VMI. This VMI was developed to have clearer resolution, so that crisper images with less blurring are produced. The primary tool used to make this high resolution possible is an electrostatic lens, which focuses ionized electrons down to a spot on the detector. If settings are correct, the lens will focus all ionized electrons with the same initial momentum to the same spot on the detector—regardless of where the ionization takes place [17]. For this initial momentum to be preserved even as the ionized electron travels toward the detector, the VMI spectrometer must be under vacuum, hence the main reason that we pumped our chamber down to a pressure of $10^{-7}$ torr. Additionally, the vacuum pressure is necessary for the detector, as this component is sensitive to open air. Within the spectrometer are three plates—a repeller, an extractor, and a ground—as well as a detector that tells us the x and y momenta of electrons ionized in the chamber. The ionization occurs with the interaction of a combined 800 nm and 400 nm laser pulse with argon gas from a gas jet. A diagram of the layout of these elements and where the laser-gas interaction occurs is shown in Figure 10. Note that the color of the pulse in this diagram does not reflect what occurs in the experiment. Our interacting field is combined 800 nm and 400 nm, rather than solely 400 nm as could be assumed from this figure.

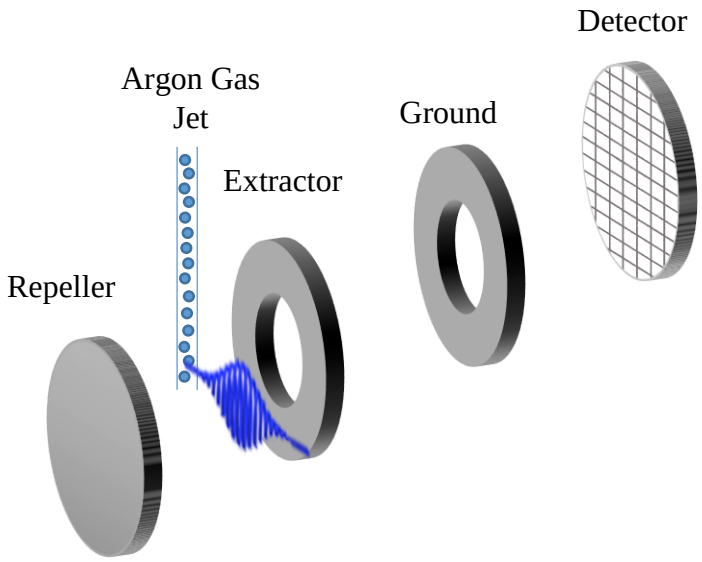


Figure 10

Layout of the velocity map imaging spectrometer. The argon gas and the laser pulse interact between the repeller plate and the extractor plate, in the ionized electrons travel through the holes in the extractor and ground plates to the detector. This entire system is in a vacuum chamber.

Voltages are applied to the repeller and the extractor plates. For the data that we take, we put the VMI in momentum mode, meaning that the voltage on the repeller is greater than the voltage on the extractor. Once ionization of the electron occurs, the voltage gradient created when we apply voltages to the repeller and extractor direct the electron through the holes in the extractor and ground plates and toward the detector. Based on their initial x and y momenta, the electrons arc as they travel past the extractor and ground plates, so their momenta are mapped on the detector. The detector consists of microchannel plates (MCPs) and a phosphor screen, both of which we apply voltages to, and we place a camera behind the detector so that we can capture images for our data.

After attaching the plates, putting them into the chamber, attaching the wires that would allow us to apply voltages to each plate, and pumping the system down to $10^{-8}$ torr, I opened the argon gas so that it could flow into the chamber, which increased the pressure in the VMI to $10^{-7}$ torr in the bottom chamber. I then adjusted the gas jet, which could be adjusted with a translation stage, until it was aligned in both the x and the y directions. I knew that it was aligned when the maximum pressure was seen on the pressure gauge for the bottom part of the VMI, as this was when the maximum amount of gas was flowing through the small orifice at the end of the jet and into the chamber. Figure 11 is the second set of data that I took for gas jet alignment, as the position at which I determined the gas jet to be most aligned in this data set is the gas jet position we used to take our SFI data.

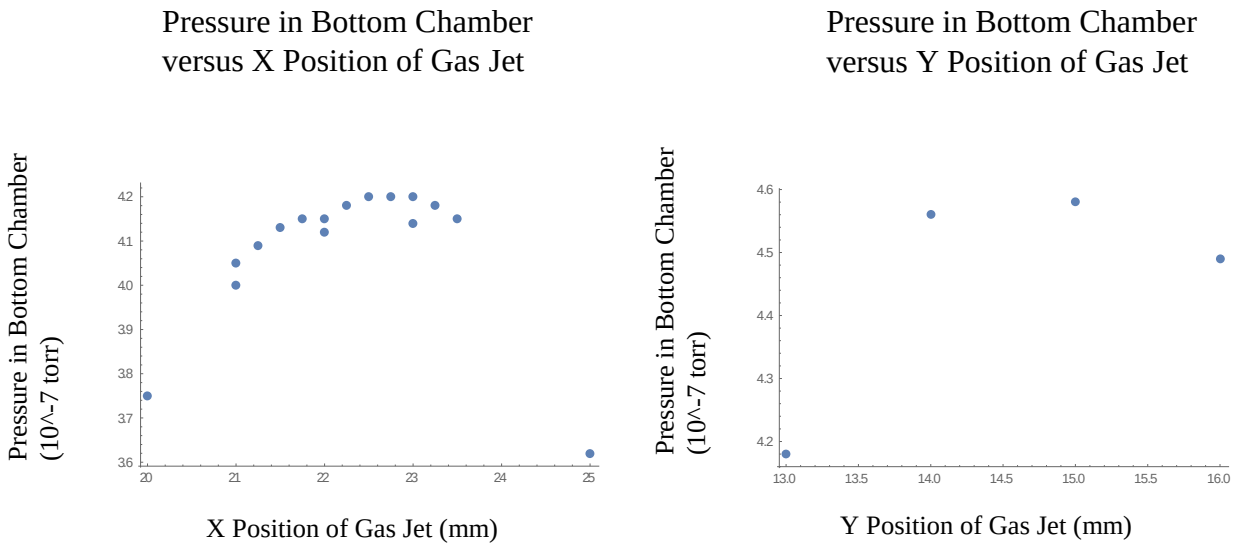


Figure 11

Experimental plots of pressure in bottom chamber of VMI spectrometer as a function of x and y positions of gas jet. The x and y points of alignment were found by determining where the pressure in the bottom chamber was highest.

The optimal x-position was 23.00 mm, and the optimal y-position was 15.23 mm. Note that there is far less data for the y-position alignment. This is because we adjusted the y-position after we interacted the laser with the gas, so that alignment would proceed more rapidly.

Next, I set up optics to send an 800 nm beam into the VMI, and aligned the laser so that it interacted with the center of the line of gas coming from the gas jet. In momentum mode, I knew that the laser was aligned when I saw several rings appear on the image taken from the detector. This meant that SFI was occurring and thus implied that the system as a whole was aligned. The image shown in Figure 12 shows these rings and an example of what should characteristically be seen when our gas jet and laser are aligned, if the laser beam is *linearly* polarized. Note that the interacting gas used to take this image is xenon, rather than argon, as xenon has a lower ionization potential so the rings can be more clearly seen. Since I was attempting to get the VMI to work as a first step, I used a gas with a lower ionization potential, ensuring that crisp rings would be seen if the gas jet and laser were aligned. For argon, we would need to send more beam power into the VMI to obtain such clear rings.

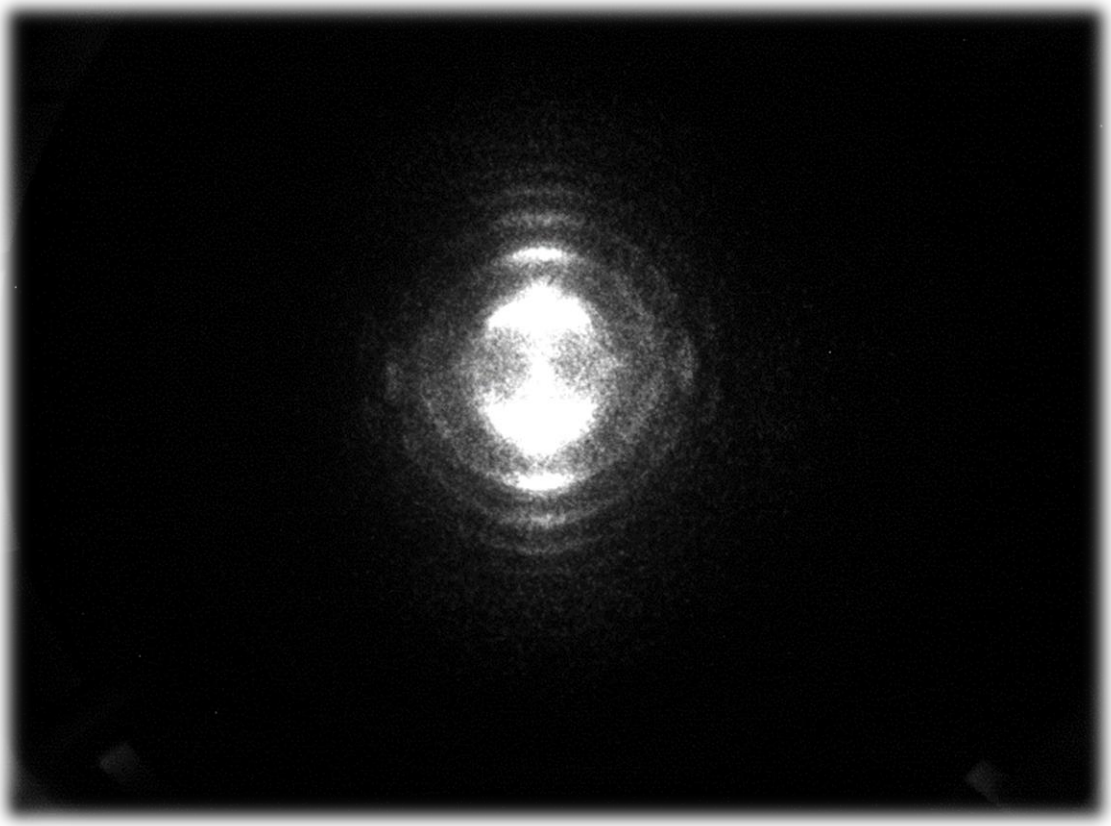

Figure 12

Experimental data taken when I interacted xenon gas with an 800 nm laser beam in momentum mode of the VMI. The crisp rings seen in the figure indicate that the gas jet and laser are well aligned, and the ratio of voltages applied on the repeller and extractor plates is accurate. Note that the rings are brighter on the y axis than on the x axis. This is because the electric field of the driving laser is polarized in the up-down direction in this case.

This image was taken when 500 V was applied to the repeller plate and 400 V was applied to the extractor plate—5/4 was the repeller to extractor voltage ratio that produced the clearest image resolution.

Each ring means an additional photon absorbed by the ionized electron beyond the minimum number needed for ionization to occur. So, the first ring around the center of Figure 12 indicates that one photon more than the minimum required for ionization was absorbed by the ionized electron. This figure shows that the VMI works, though a more rigorous characterization would include the minimum input power for ionization to occur, the voltages that the MCPs and phosphor screen were set to be at, and images taken with a few other input gases with higher ionization potentials (such as xenon and krypton).

### 2. Optics setup

Figure 13 shows a sketch of parts of the optics setup for this experiment. There are several optics, such as wave plates and polarizers, which are not shown in this figure that came after the first dichroic mirror and prior to any optics contained in the dotted box. All parts of the sketch within this dotted box are optics that I set up.

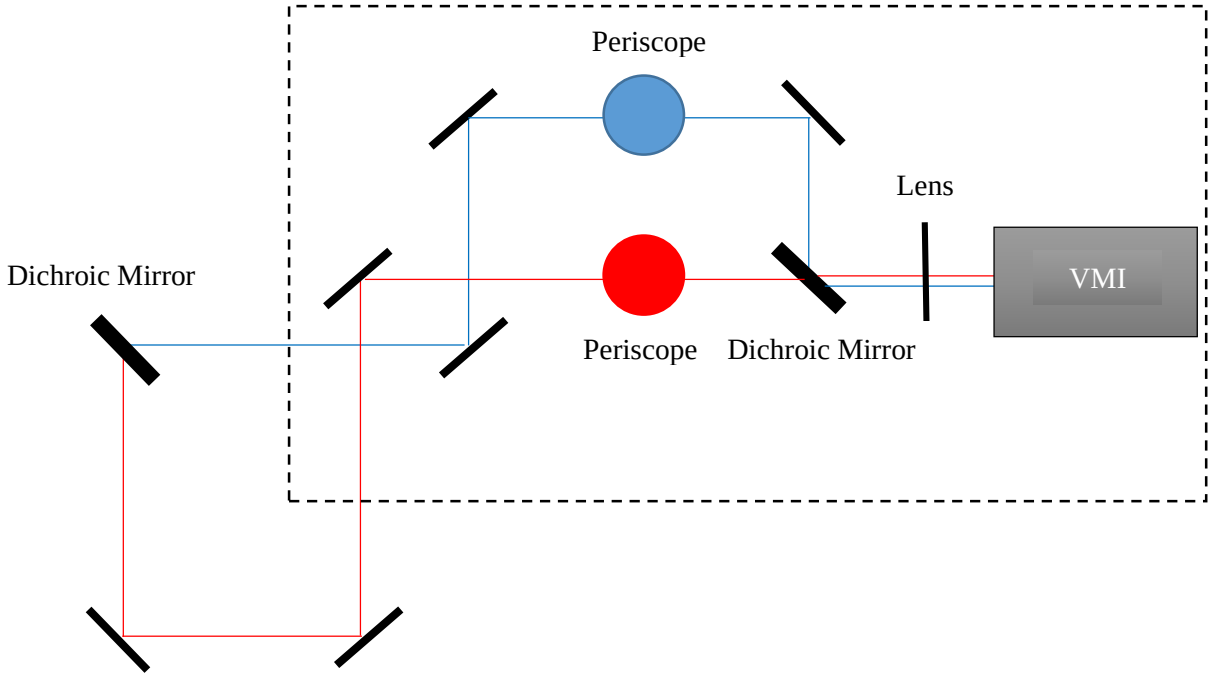


Figure 13

Part of the optics setup for this experiment. The parts that I set up are contained in the dotted box, and serve to take the already circularly polarized 800 nm and 400 nm beams, increase the heights of these beams to match that of the VMI window, recombine the beams at a dichroic mirror, and focus them into the VMI. The circular polarization optics come before the optics that I set up.

One important constraint for this setup that should be mentioned is that the total path lengths of the 800 nm and 400 nm beams from the first dichroic mirror to the second must be equal. This is because of our requirement of temporal overlap. If one beam path is shorter than the other (on the order of tens of microns), then the 800 nm and 400 nm will not arrive at the center of the VMI chamber at the same time, so two-color SFI would not occur. A note on the sketch in Figure 13 is that the periscopes are in place to increase the height of the beams. The laser emitting the original 800 nm is at a lower height than the window entrance into the VMI, so I took this into account by using periscopes. An additional note is that the lens in the sketch is on a translation stage, which allows us to slightly adjust where the lens focuses the 800 nm and 400 nm beams such that the focus point is exactly in the center of the VMI.

### 3. Camera and stage control

Although a program previously existed which was able to take basic static images, I rewrote the program to be able to interface a delay stage and take the necessary series of images to perform a tomographic reconstruction. In Figure 14, all parts that I modified from the original program, on the control panel, are outlined in dotted boxes.

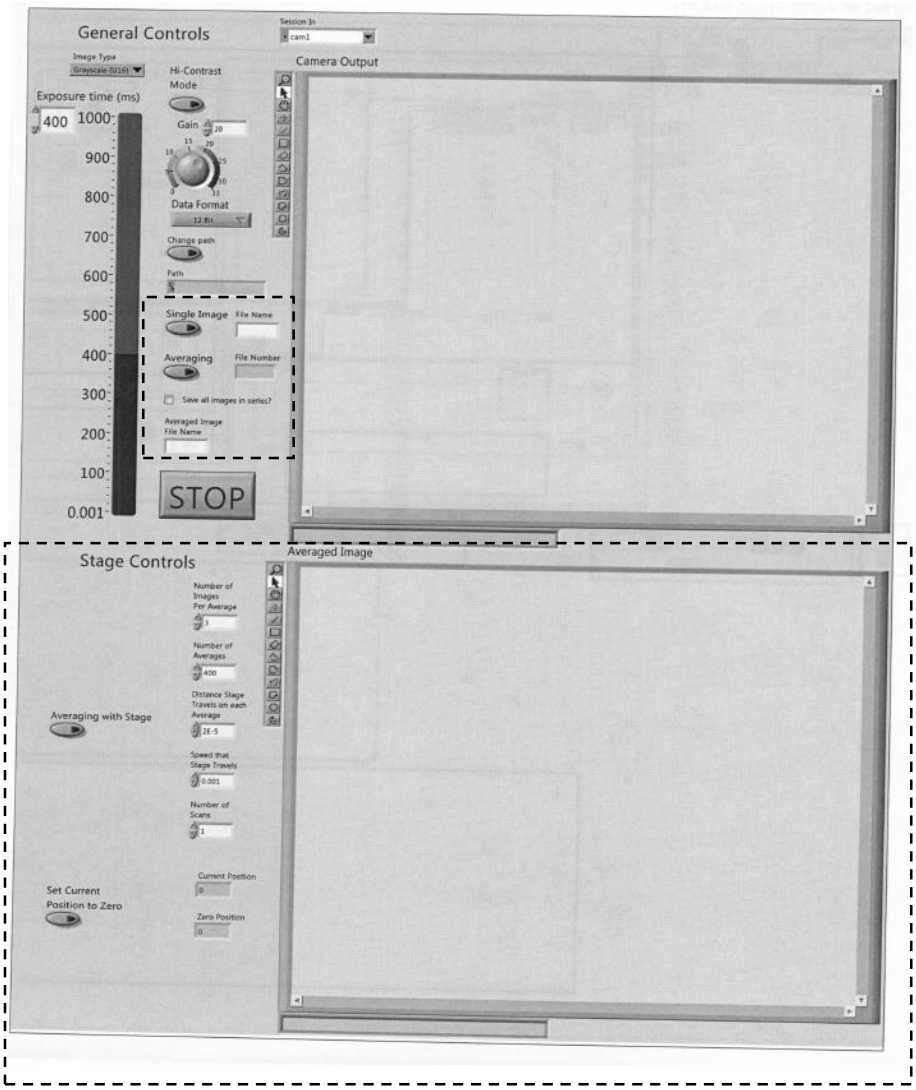


Figure 14

Printout of control panel of the program we used to run scans for this experiment. We can use this program to control the camera imaging SFI and to control the translation stage inducing phase delay between the 800 nm and 400 nm beams. I added to the original program the features outlined with dotted boxes.

The first new feature that I added was an averaging capability, where one can click a button, take a series of images, average these images, and save the average in a file. The averaging feature was then incorporated into our main addition—moving the delay stage incrementally and taking an average image at each stage position. With this capability, we are able to find and set a zero position of the stage, set the incremental amount that the stage moved for each loop of the program, and choose the number of loops. We can also select how many images to take and average at each stage position, and the program will save the average images in a file. Since a scan of 400 movements of the stage could take around 20 minutes, it is convenient that this program automatically performs an entire scan so that we can complete other work in the lab while the scan is running. With this series of average images that each correspond to a time (and consequently

phase) delay, we can proceed to perform a tomographic reconstruction of the photoelectron distribution.

# V. Results and Analysis

## A. Normalized sinograms

Once we have an averaged image corresponding to each time delay—in other words, an image for each position that we moved the stage to—we can combine and manipulate this series of images in MATLAB. To produce a normalized sinogram, we first compress each image obtained to a single vertical vector, where each vector is the corresponding image integrated over each row. Then, the vectors for each image are concatenated to make a single image of momentum in the y-direction as a function of time delay. For this experiment, our time delay increment was 133 attoseconds. Then, the image is normalized by dividing each value in a column vector by the largest value in that column vector. This normalization compensates for the points in time when the 800 nm and 400 nm pulses are not maximally overlapped and therefore the total peak pulse power is not maximal, so the images produced may not be as bright. Finally, a difference from average is taken, which allows us to distinguish those electrons that are ionized but do not return to their parent atom from those that rescatter. Our experimental and theoretical normalized sinograms for both the counter-rotating case and the co-rotating case are shown in Figure 15.

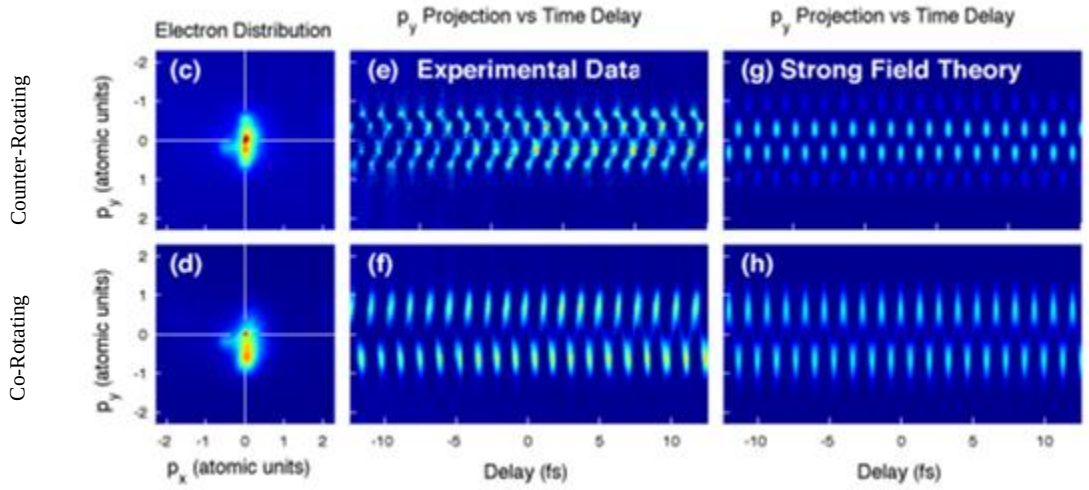


Figure 15
(Mancuso *et al*, 2015)
Experiment and theory sinograms in the counter-rotating and co-rotating cases used for our paper.

We will use these sinograms, with their corresponding time delays, to perform a tomographic reconstruction.

## B. Tomographic reconstructions

There is a function, called iRadon (inverse Radon transform), in MATLAB that does a tomographic reconstruction on an array like a raw sinogram image, if given the correct phase delay increment. This increment can be found from taking a lineout of the sinogram, fitting a sinusoidal

function to the lineout, and finding the phase angle from the fit function. Figure 16 shows these reconstructions.

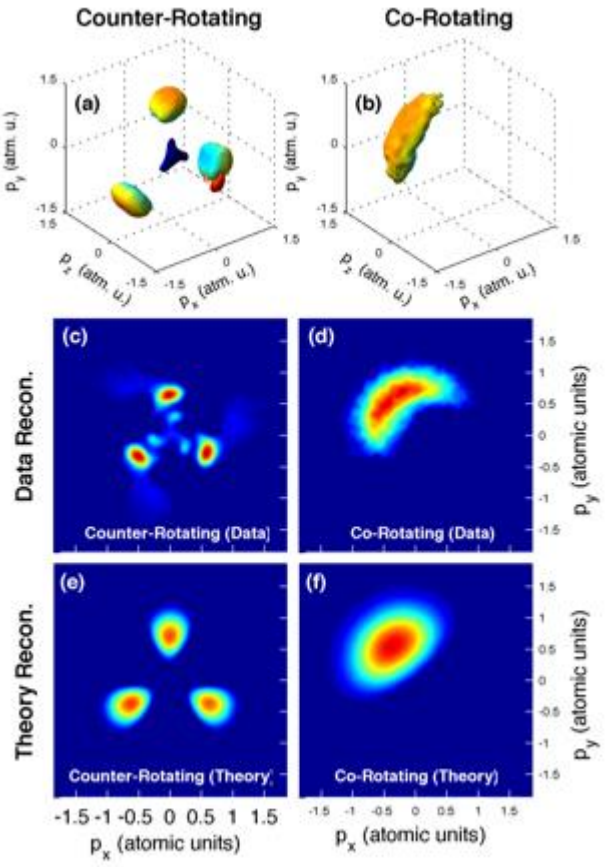


Figure 16
(Mancuso *et al*, 2015)
(a) and (b) 3D experimental tomographic reconstructions from our paper, for the counter-rotating and co-rotating cases. (c)-(e) experimental and theoretical 2D projections of tomographic reconstructions for both cases. An important feature seen in these sets of images is the presence of low-energy structures in the counter-rotating case.

## C. Implications of results

Notice that in the refined tomographic reconstructions, the trefoil pattern in the counter-rotating case and the cardioid in the co-rotating case can be seen clearly, and in many ways match the theory reconstructions. However, one notable difference between data and theory in the counter-rotating case is the presence of low-energy structures. These structures correspond to rescattering of ionized electrons off of the Coulomb potential of their parent atom, which implies that these ionized electrons come close to recombining with their parent atoms. Such low-energy features are not present in the co-rotating case [16].

To ensure that these low energy structures are certainly an artifact of rescattering of electrons off the Coulomb potential of their parent atoms, we generated time-dependent Schrödinger equation (TDSE) simulations to observe the effects of screening versus not screening the Coulomb potential in the counter-rotating and co-rotating cases. The results are shown in Figure 17.

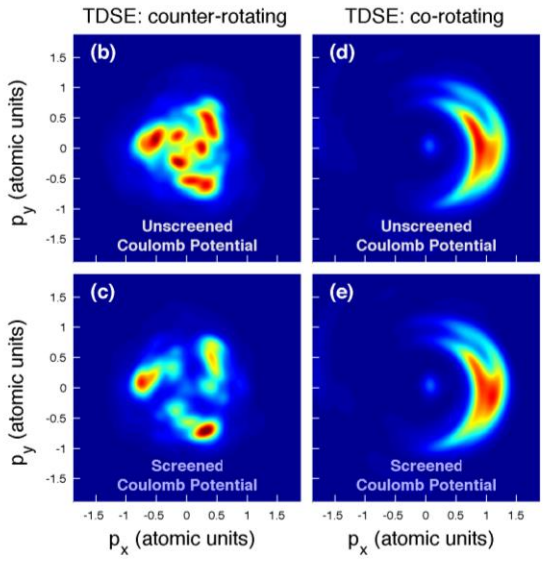


Figure 17
(Mancuso *et al*, 2015)
TDSE simulations of the unscreened versus screened Coulomb potential in the counter-rotating and co-rotating cases.

In Figure 17, the co-rotating case shows no difference between the screened and unscreened Coulomb potential. However, the counter-rotating case reveals low-energy features when the Coulomb potential is unscreened that are not present when this potential is screened. This leads us to further believe that the low-energy structures in the counter-rotating case in Figure 16 are in fact a result of rescattering of ionized electrons off the Coulomb potentials of their parent atoms.

From this knowledge, we can understand why high harmonic generation, where ionized electrons recombine with their parent atoms, can take place in the counter-rotating case, but cannot in the co-rotating case. Additionally, we know that by using circularly polarized driving laser fields, we can more distinctly separate those electrons that are ionized but do not return to their parent atoms from those that return and rescatter off their parent atoms.

# VI. Conclusions

In this thesis, I explained our objective of using two-color circularly polarized driving fields for SFI in a VMI spectrometer, and using tomographic reconstruction techniques to reconstruct the photoelectron distribution from the counter-rotating and co-rotating cases. After discussing some applications of circular harmonics in measuring magnetic material properties and chirality, I went over the concepts of high harmonic generation, strong field ionization, and two-color circularly polarized light fields. I mentioned experiments that have successfully produced circularly polarized high harmonics, and delved into further detail regarding the applications of circular

HHG. Next, I overviewed the experimental setup and explained the role of phase delay. I honed in on what my specific roles were for this experiment, including the setup of the VMI, my contribution to the optics setup, and my modifications to a LabView code controlling the camera we used to image SFI and the translation stage that induced the necessary phase delays. In the results, I showed plots and images that my lab mates and I had generated from the images we took in the VMI. Finally, I explained the significance of what we identified in our reconstructions in experimentally determining why circularly polarized high harmonics can be produced with counter-rotating driving laser fields.

# VII. Further work

Currently, I am involved with several projects building on this core experiment, including: taking scans of SFI occurring with varying relative intensities of the 800 nm and 400 nm light, creating a mechanism that detects the exact polarization of the light entering the VMI, and restructuring the original optics setup to be more compact.

## A. Varying relative intensities

In the original experiment, the intensities of the 800 nm beam and 400 nm beam were the same. We are experimenting with changing the relative intensity of the 800 nm and 400 nm beams to observe any possible trends in our reconstructions that are a function of these intensity variations. It is relatively simple to change the intensities of each beam—a turn of a specific wave plate in the laser and a couple of the wave plates that circularly polarize the beams can change the intensity of one or both beams. We want to perform this experiment to understand how we can control electron trajectories after the electrons are ionized, and how we can vary the intensities to get stronger rescattering. In our preliminary data, shown in Figure 18, we see evidence that increasing the 400 nm light to be more intense than the 800 nm light will lead to stronger rescattering.

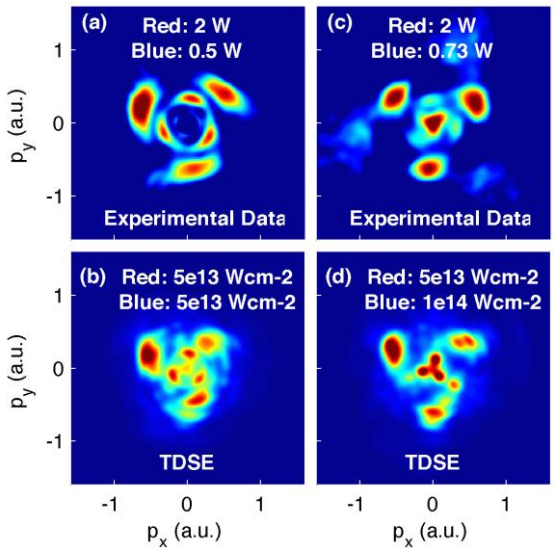


Figure 18

(Mancuso and Hickstein, 2015)

(a)-(b) Experimental data, with the 800 nm light at 2 W of power and the 400 nm light being increased. Notice that the low energy structures in (b) are closer to the center than those in (a), indicating stronger rescattering. (c)-(d) TDSE simulations showing that if intensity of 400 nm light is higher than that of 800 nm light, there will be stronger rescattering.

## B. Polarization detector

One issue that we have run into during our experiment thus far is that we cannot tell when the 800 nm and 400 nm beams are perfectly circularly polarized. If the beams are circular, and we put a polarizer at the end of our beam line and a power meter behind the polarizer, the power should stay constant as we rotate the polarizer. However, the power meter fluctuates so much that small changes are not easily noticed, and it is extremely difficult to tell with the naked eye whether the beam maintains a constant intensity when we turn the polarizer. Thus, I am developing a polarization detector that uses a photodiode to determine whether the intensity of the beam changes as the polarizer rotates. My detector will interface a photodiode and a rotational stage with LabView, and will produce a plot of the voltage detected by the photodiode as a function of the angle that the rotational stage is at. The λ/4 wave plate that is rotated to adjust the ellipticity of the driving field light will be on the rotational stage, and the code will cycle through 60 degrees of the wave plate and determine at which degree the photodiode voltage stays constant over a full rotation of the polarizer. Since the photodiode voltage will not fluctuate as much as the power meter reading (we will choose a photodiode with a slightly longer response time) but can detect small changes in the beam power, we will have a much more accurate reading of the wave plate settings that make both of our beams perfectly circularly polarized.

## C. Restructuring of optics setup

Currently, the optics setup is slightly unstable and involves several optics that are not essential to produce circular beams. I am working to restructure the setup such that we use the minimum number of optics required, shorten the path lengths of the beams, and ensure that the path length of each beam is equal. Using minimal optics and having shorter path lengths will reduce the instability from our current setup. I also added an 800 nm pump beam to the setup, which will enable us to align molecules when we use this setup to study SFI with molecular gases in the near future. An AutoCAD drawing of the new setup is shown in Figure 19 below.

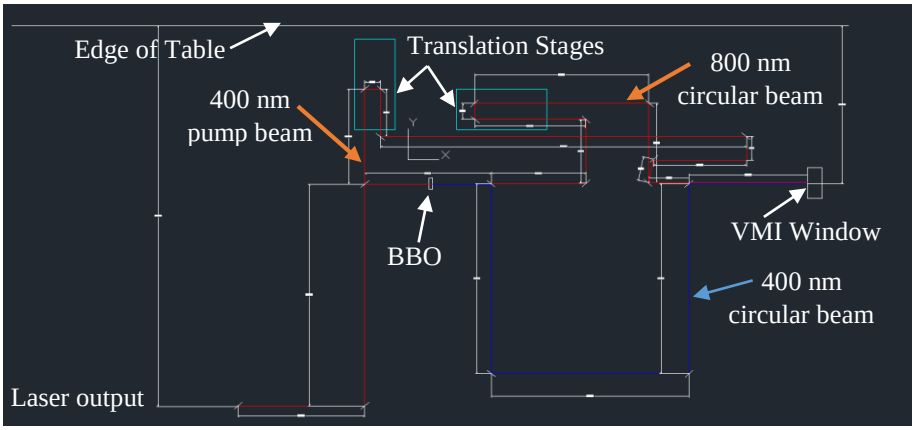


Figure 19

Restructuring of optics setup. All white lines not labeled otherwise are indicating distances between optics. Note that wave plates, polarizers, and lenses are not included in this diagram. Those will be placed after we ensure that this setup works on the table as anticipated.

This setup is not necessarily finalized, but we will utilize it to start and make adjustments as needed.

# VIII. Acknowledgments

This research was a large collaboration, and would not have been possible without each and every one of their contributions. First and foremost, I would like to thank Dr. Kapteyn and Dr. Murnane, my advisers, for their support and their dedication to ensuring the success of this experiment. I would not have had the opportunity to work on this experiment and learn all of the knowledge I displayed in my thesis without the guidance of Chris Mancuso, one of the graduate students that work in the Kapteyn-Murnane lab. Other graduate students and post-docs that I worked closely with for this experiment and that helped me considerably are Dr. Dan Hickstein, Dr. Patrik Grychtol, Dr. Ronny Knut, Dr. Franklin Dollar, and Dmitriy Zusin. In addition to those I worked with in the lab, I want to thank my family, friends, and professors, within and outside of physics, who supported me throughout every step of my undergraduate physics career. Cheers to a fantastic four years!

# IX. References


[1] Schmidt, W. Ultra-fast nuclear detonation pictures. *ThisAndThat Website*. Retrieved from http://www.bibliotecapleyades.net/ciencia/ciencia_uranium06.htm

[2] Toon, J. (2014). Silicon-germanium chip sets new speed record. *Georgia Tech*. Retrieved from http://www.news.gatech.edu/2014/02/17/silicon-germanium-chip-sets-new-speed-record

[3] Vrakking, M. (2006). Direct and indirect methods to study attosecond timescale electron dynamics. *Physica Scripta, 73.* doi: 10.1088/0031-8949/73/1/N07

[4] Kfir, O., Grychtol, P., Turgut, E., Knut, R., Zusin, D., Popmintchev, D… Cohen, O. (2014). Generation of phase-matched circularly-polarized extreme ultraviolet high harmonics for magnetic circular dichroism spectroscopy. *Nature Photonics, 9.* doi: 10.1038/nphoton.2014.293

[5] An introduction to circular dichroism spectroscopy. *University of California, Irvine.* Retrieved from http://www.chem.uci.edu/~dmitryf/manuals/Fundamentals/CD%20spectroscopy.pdf

[6] Gühr, M. What is high harmonic generation? *Stanford University*. Retrieved from http://web.stanford.edu/~mguehr/research_HHG.html

[7] Popmintchev, T., Chen, M-C., Arpin, P., Murnane, M.M & Kapteyn, H.C. (2010). The attosecond nonlinear optics of bright coherent x-ray generation. *Nature Photonics, 4.* doi: 10.1038/nphoton.2010.256

[8] Ishikawa, K.L. (2010). High-harmonic generation. *Advances in Solid State Lasers Development and Applications.* Retrieved from http://ishiken.free.fr/english/lectures/HHG.pdf

[9] Hickstein, D.D. (2014). Photoelectron and photoion spectroscopy of atoms, nanoparticles, and nanoplasmas irradiated with strong femtosecond laser pulses. *Kapteyn-Murnane Group Thesis Defense.*

[10] Corkum, P.B. (1993). Plasma perspective on strong-field multiphoton ionization. *Physical Review Letters, 71,* 1994-1997. Retrieved from http://journals.aps.org/prl/pdf/10.1103/PhysRevLett.71.1994

[11] Dietrich. P., Burnett, N.H., Ivanov, M. & Corkum, P.B. (1994). High-harmonic generation and correlated two-electron multiphoton ionization with elliptically polarized light. *Physical Review A, 50.* Retrieved from http://journals.aps.org/pra/pdf/10.1103/PhysRevA.50.R3585

[12] Long, S., Becker, W. & McIver, J.K. (1995). Model calculations of polarization-dependent two-color high-harmonic generation. *Physical Review A, 52,* 2262-2278. Retrieved from http://journals.aps.org/pra/pdf/10.1103/PhysRevA.52.2262

[13] Vodungbo, B., Sardinha, A.B., Gautier, J., Lambert, G., Valentin, C., Lozano. M… Zeitoun, P. (2011). Polarization control of high order harmonics in the EUV photon energy range. *Optics Express, 19,* 4346-4356. doi: 10.1364/OE.19.004346.

[14] Fleischer, A., Kfir, O., Diskin, T., Sidorenko, P. & Cohen, O. (2014). Spin angular momentum and tunable polarization in high-harmonic generation. *Nature Photonics, 8*, 543-549. doi: 10.1038/NPHOTON.2014.108.

[15] Mancuso, C. & Hickstein, D.D. (2014) Photoelectron distributions from two-color circularly polarized fields. *Kapteyn-Murnane Group Meeting Presentation.*

[16] Mancuso, C., Hickstein, D.D., Grychtol, P…Gopalakrishnan, M…Murnane, M.M. (2015). Strong field ionization with two-color circularly polarized laser fields. *Physical Review A, 91.* doi: http://dx.doi.org/10.1103/PhysRevA.91.031402.

[17] Eppink, A.T. J. B. & Parker, D.H. (1997). Velocity map imaging of ions and electrons using electrostatic lenses: Application in photoelectron and photofragment ion imaging of molecular oxygen. *Review of Scientific Instruments, 68,* 3477-3484. doi: 10.1063/1.1148310.